Ocean Engineering 309 (2024) 118458

Contents lists available at ScienceDirect

Ocean Engineering

journal homepage: www.elsevier.com/locate/oceaneng

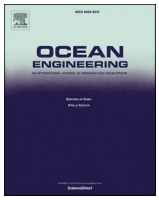

Research paper

GWSM4C: A global wave surrogate model for climate simulation based on a convolutional architecture

Quan Jin [a,b], Xingjie Jiang [b,c,d], Feng Hua [a], Yongzeng Yang [b,c], Shumin Jiang [b,c], Chen Yu [e], Zhenya Song [b,c,d,*]

[a] Guangdong Provincial Key Laboratory of Marine Disaster Prediction and Prevention, Shantou University, Shantou, 515063, China
[b] First Institute of Oceanography and Key Laboratory of Marine Science and Numerical Modeling, Ministry of Natural Resources, Qingdao, 266061, China
[c] Shandong Key Laboratory of Marine Science and Numerical Modeling, Qingdao, 266061, China
[d] National Engineering Laboratory for Integrated Aero-Space-Ground-Ocean Big Data Application Technology, Xi'an, 710072, China
[e] Research Department, Computing Product Line, ICT Product & Solution, Huawei Technologies Co. Ltd., Hangzhou, 310052, China

ARTICLE INFO

Keywords:
Significant wave height
Convolutional neural network
Wave propagation
Climate simulation

ABSTRACT

Accurate and rapid ocean surface wave simulations are essential for navigation safety, marine activity, and climate change research. However, traditional numerical wave models incur substantial computational costs, especially in long-term simulations for climatology research. Deep-learning methods have shown promise in enabling faster simulations with fewer computational resources. However, the cumulative error in current deep-learning wave models limits their use as surrogate component models in climate modeling. In this work, a deep-learning model, named the Global Wave Surrogate Model for Climate simulation (GWSM4C), was developed based on a convolutional architecture, which accounts for the physical processes (wind waves and swells) of waves. Because GWSM4C can automatically generate initial conditions for each simulation moment depending only on historical wind fields, the accumulation of errors from previous simulated wave states can be avoided. The experimental results demonstrated that simulated global significant wave height produced by GWSM4C exhibited a correlation coefficient of 0.94 and a root-mean-square error of 0.21 m compared with the traditional numerical wave model. Furthermore, the generalization test of the GWSM4C indicates that it is feasible to use GWSM4C for long-term wave simulation in climatology-related studies or to integrate it into a coupled climate model as a surrogate wave component model.

1. Introduction

Ocean surface waves (hereafter called wave) can originate from wind events that occur locally (wind waves) or remotely (swells), which can travel thousands of kilometers and vary in height from a few centimeters to tens of meters, carry enormous amounts of energy and play a crucial role in pelagic navigation (Trulsen et al., 2015; Waseda et al., 2014), fishing (Tamura et al., 2009; Waseda et al., 2012), coastal activities (Dong et al., 2020; Wang et al., 2020), oil exploration (Cavaleri et al., 2016; Magnusson and Donelan, 2013; Soares et al., 2003), and climate systems (Hemer et al., 2012; Young and Ribal, 2019).

Currently, numerical simulations of third-generation wave models, such as WAM (WAMDI Group, 1988), WaveWatchIII (Tolman, 1991; Tolman and Chalikov, 1996), and SWAN (Booij et al., 1999; Ris et al., 1999), remain the primary methods used to perform global or regional wave simulations and forecasts. These wave models are all based on the wave energy/action balance equation, which solves each wave element iteratively by considering the principal wave driver, i.e., the wind, with preset boundary conditions. However, the wave energy/action balance equation must be solved for each two-dimensional wave spectrum at each spatial grid point and for each iterative step, resulting in an enormous consumption of computational resources in both fast predictions and long-term wave simulations.

Recently, the development of machine learning (including deep learning) algorithms has triggered the emergence of new empirical statistical methods for wave forecasting at a single point or within small areas. For example, James et al. (2018) predicted significant wave heights (SWHs) using the multilayer perceptron (MLP) method in deep

* Corresponding author. First Institute of Oceanography and Key Laboratory of Marine Science and Numerical Modeling, Ministry of Natural Resources, Qingdao, 266061, China.
E-mail address: songroy@fio.org.cn (Z. Song).

https://doi.org/10.1016/j.oceaneng.2024.118458
Received 24 March 2024; Received in revised form 28 May 2024; Accepted 9 June 2024
Available online 14 June 2024

neural networks, which yielded improved results compared with those generated by the traditional SWAN model in terms of both computational efficiency and SWH accuracy. In such research, the initial wave state is typically considered to be known and accurate, indicating that the prediction has a temporal limit of only a single time step. Subsequently, time series models such as recurrent neural networks (RNNs) and the long short-term memory (LSTM) method were used for longer-term prediction. Feng et al. (2022) predicted SWH in the East and South China seas for the subsequent 1, 3, 6, and 24 h with the LSTM and gate recurrent unit (GRU) methods and acquired fewer errors than accumulated when performing the same prediction with traditional recurrent neural networks. In the context of single-point prediction models, it is necessary to iterate the model to simulate predictions for broader marine areas. Zhou et al. (2021b) employed the ConvLSTM algorithm to perform short-term forecasts of SWH in the South China Sea. Models of this type have the combined characteristics of a convolutional neural network (CNN) and LSTM, providing them with the capabilities of short-term prediction and wider coverage in a single forecast. However, their performance in predicting extreme sea conditions is somewhat limited owing to the lack of such conditions in the training data. Wang et al. (2022) improved the prediction of extreme sea conditions by utilizing a CNN-BiLSTM-Attention model and incorporating training data that included extreme sea conditions. Alizadeh and Nourani, 2024 used wave age and swell data as inputs for wave forecasting and hindcasting in the southern Caspian Sea using the GRU and LSTM models.

The time-series-based approaches used in wave simulations still rely heavily on the given initial wave states, which can result in cumulative errors beyond control with increasing iterations. Moreover, current models are generally limited by uneven distributions of extreme and common wave conditions in their training datasets, which can in turn affect the prediction results. The above drawbacks associated with deep learning models result from the failure to explicitly characterize wave propagation. Thus, such models are incapable of capturing both the influence of wave energy propagating from other areas and the effect of complex interactions between locally and nonlocally generated waves in large water bodies, e.g., in the context of a global wave environment.

This study developed a new deep-learning model for SWH simulation called the Global Wave Surrogate Model for Climate simulation (GWSM4C). This new model can simultaneously update the initial conditions for each simulation moment using historical wind fields, which means that the accumulation of errors from a previous simulated wave state can be avoided. These characteristics indicate that GWSM4C can be used in long-term wave simulations in climatology-related studies.

The remainder of this paper is organized as follows. In Section 2, the dataset, model structure, evaluation metrics, and details regarding the training and testing of the GWSM4C are presented. Section 3 provides a comprehensive evaluation and analysis of the simulation ability of GWSM4C, and Section 4 discusses certain key characteristics of GWSM4C. Finally, the conclusions are presented in Section 5.

2. Datasets and methods

2.1. Datasets

In this study, the training and testing datasets comprised global hourly SWH generated by the numerical wave model (MASNUM-WAM) developed by the Key Laboratory of Marine Science and Numerical Modeling, with forcing wind fields derived from hourly data of the fifth generation of the European Center for Medium-Range Weather Forecasts (ECMWF-ERA5) reanalysis datasets (Hersbach et al., 2020; Bell et al., 2021).

MASNUM-WAM is a third-generation wave model. It solves the energy spectrum balance equation in wavenumber space and uses a complicated inlaid scheme in spherical coordinates to simulate shoaling and refraction effects in shallow waters, the modulation effect of the background current on wave evolution, and the refraction of waves propagating along great circle paths (Yuan et al., 1991, 1992; Qiao et al., 2016; Jiang et al., 2023). MASNUM-WAM has become widely accepted in scientific and engineering fields (Bao et al., 2020; Jiang et al., 2016; Sun et al., 2017), and it has evolved as a pivotal component of certain operational ocean forecasting systems (OFSs) (Wang et al., 2016; Qiao et al., 2019).

This study adopted source functions from the ST6 package (Liu et al., 2017; Rogers et al., 2012; Zieger et al., 2015), which considers the effects of wind input, white-capping dissipation, and swell dissipation on the evolution of waves. Additionally, the DIA scheme (Hasselmann et al., 1985a; 1985b) was employed to quantify the nonlinear energy transfer among waves. The wave model adopted a global computational grid that spanned the region 80°S–80°N, 0°–359.5°E, with 0.5° × 0.5° horizontal resolution. The spectral space was set to 24 directions in intervals of 15°, and 35 wavenumbers were arranged logarithmically from the lower threshold of 0.0071 to the upper limit of 4.6341, with intervals characterized by $k_i/k_{i+1} = 1.21$, which is equivalent to frequencies of 0.042 Hz–1.073 Hz, with a ratio of 1.1 at infinite depth.

The ERA5 hourly forcing winds provide the zonal (u) and meridional (v) wind components at a height of 10 m above the sea surface with a horizontal resolution of 0.25° × 0.25°. The bathymetric data were derived from the ETOPO1 (Amante and Eakins, 2009) dataset published by the National Oceanic and Atmospheric Administration National Geophysical Data Center. The shoreline data were procured from the Global Self-consistent, Hierarchical, High-resolution Geography Database (Wessel and Smith, 1996).

2.2. GWSM4C model

As shown in Fig. 1, the GWSM4C architecture comprises two key processes: spatiotemporal feature extraction (STE) and instantaneous feature extraction (IE). Given that the initial wave state at any specific moment is a product of historical winds, GWSM4C arranges several STE structures to generate the initial conditions for the simulation time (T - 0 h, h represents hours) using the wind fields at previous times (i.e., T - 72, T - 66, …, T - 6 h). Based on the initial conditions presented by the STEs, the other key component (IE) is employed to estimate the instantaneous local waves adopting the winds at time T - 0 h. Through these two processes, the spatiotemporal and instantaneous features of SWH in large sea areas, e.g., the global oceans, can be well estimated.

In GWSM4C, each STE embodies a neural network architecture of L_{num} layers, and each layer contains 48 convolutional kernels of size 3 × 3. The number of layers L_{num} can limit the range of the receptive field (RF), and the RF range determines the size of the area within which the waves propagate. According to the effective RF proposed by Luo et al. (2016), wherein any pixel with a value > 4.55% of the central point is deemed within the RF, the following relationship between L_{num} and RF can be obtained:

$$log_{10}L_{num} = \frac{log_{10}\,RF - log_{10}\,10}{0.56} + log_{10}\,5 \tag{1}$$

Then, the RF can be calculated as follows:

$$RF = (2P_{dis}) \cdot 2 + 1 \tag{2}$$

with the maximum propagation distance expressed as follows:

$$P_{dis} = \frac{C_{g.p} \cdot T_{travel}}{L_{dis}} \tag{3}$$

where $C_{g.p}$ indicates the group speed of the primary wave energy, T_{travel} denotes the travel time of $C_{g.p}$, and L_{dis} is the unit longitudinal-latitudinal length. Therefore, to fit the features of wave propagation, the value of L_{num} in each STE should be designed according to $C_{g.p}$ and T_{travel}. Through Eqs. (1)–(3), the key characteristics of the main wave energy, i.

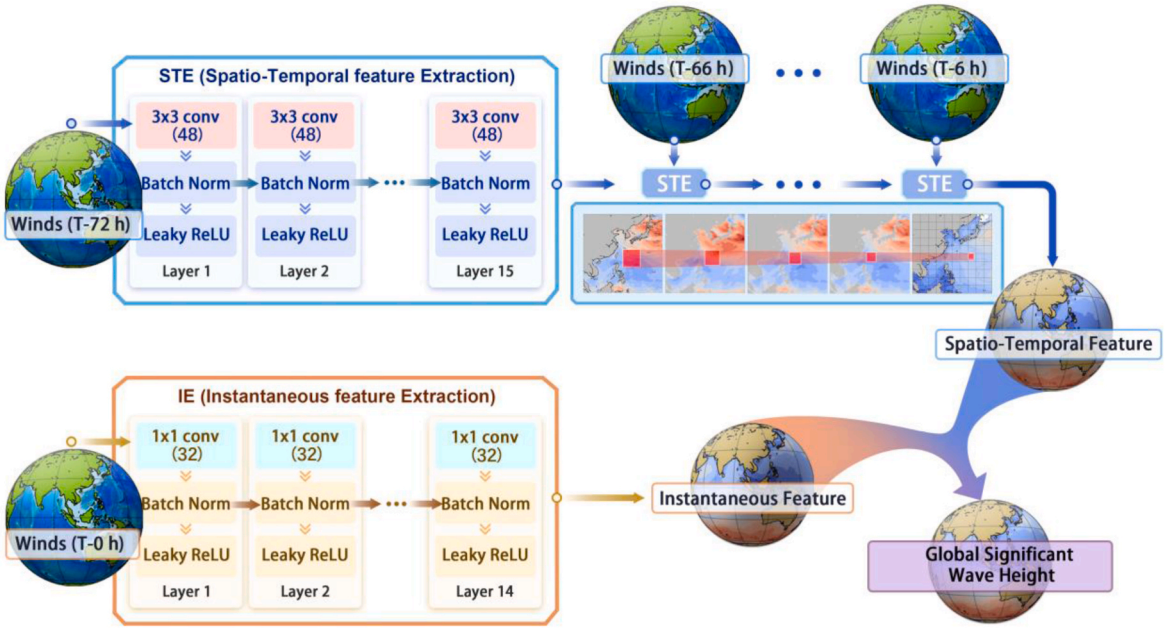

Fig. 1. GWSM4C architecture.

e., the propagation velocity and distance, are involved in the convolutional iterations and can be learned by the STEs in the training process.

To prevent high-speed main waves from passing through the designed RF in T_{travel}, the maximum possible value of $C_{g,p}$ should be adopted. By introducing the PM spectrum (Pierson Jr and Moskowitz, 1964)

$$S(\omega) = \frac{\alpha g^2}{\omega^5} exp - \beta\left(\frac{g}{U\omega}\right)^4 \tag{4}$$

The corresponding peak frequency ω_p, where the primary wave energy is concentrated, can then be related to the wind speed U as follows:

$$\omega_p = \left(\frac{4}{5}\right)^{\frac{1}{4}} g\frac{\beta^{\frac{1}{4}}}{U} \tag{5}$$

In Eqs. (4) and (5), U is the wind speed at a height of 19.5 m above the sea surface, g is the gravitational acceleration ($= 9.81$ m/s^2), and α ($= 8.10 \times 10^{-3}$) and β ($= 0.74$) are constants. Through the dispersion relationship in deep water, ω_p can be related to the peak wavenumber k_p:

$$\omega_p^2 = gk_p \tag{6}$$

Then, the group velocity $C_{g,p}$, namely, the propagation speed of the main wave energy, can be obtained as follows:

$$C_{g,p} = \left.\frac{\partial\omega}{\partial k}\right|_{\omega=\omega_p} = \frac{U}{2\left(\frac{4}{5}\right)^{\frac{1}{4}}\beta^{\frac{1}{4}}} \tag{7}$$

According to the maximum wind speed in the training dataset (see Section 2.4), the fastest possible group velocity can reach 22.5 m/s. Notably, waves at frequencies lower than the peak might propagate faster, but the energy contained in such waves can be ignored in comparison with that in the peaks.

Fig. 2 depicts the relationship between T_{travel} and the required value of L_{num} with $C_{g,p} = 22.5$ m/s and $L_{dis} = 111$ km (i.e., the length of one transmeridional degree on the equator). As shown in Fig. 1, the STE is employed several times to capture the spatial characteristics of the SWH at different historical moments. The intervals of those moments should be set to confirm T_{travel}, thereby allowing the wave propagation features

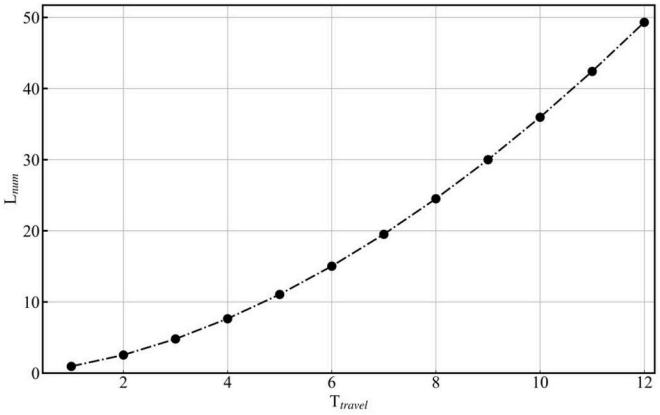

Fig. 2. Relationship between T_{travel} and the required value of L_{num} at $C_{g,p} = 22.5$ m/s and $L_{dis} = 111$ km.

in the RF to be learned. Considering the computational efficiency, because additional layers incur greater computational costs and the traditional wind simulation interval is 6 h, T_{travel} in GWSM4C is set to 6 h, corresponding to a configuration of 15 layers (i.e., $L_{num} = 15$) according to Fig. 2.

The IE structure in GWSM4C is designed to extract the characteristics of instantaneous waves under wind fields at T - 0 h. The number of layers in the IE structure is set to 14, and each layer contains 32 convolution kernels. The size of each kernel is set at 1×1.

2.3. Evaluation metrics

In this work, the data from the MASNUM-WAM simulation are treated as true values, and the emulation ability of the GWSM4C model is evaluated using the correlation coefficient (COR), root mean square error (RMSE), bias (BIAS), and relative error (RE). The above evaluation indicators are expressed as follows:

$$COR = \frac{\sum_{i=1}^{n}(y_i - \bar{y})(x_i - \bar{x})}{\sqrt{\sum_{i=1}^{n}(y_i - \bar{y})^2}\sqrt{\sum_{i=1}^{n}(x_i - \bar{x})^2}} \tag{8}$$

$$RE = \frac{1}{n}\sum_{i=1}^{n}\frac{|x_i - y_i|}{x_i} \tag{9}$$

$$RMSE = \sqrt{\frac{1}{n}\sum_{i=1}^{n}(y_i - x_i)^2} \tag{10}$$

$$\mathrm{BIAS} = \frac{1}{n}\sum_{i=1}^{n}(x_i - y_i) \tag{11}$$

where x_i and y_i denote the SWH values output by MASNUM-WAM and GWSM4C, respectively. Subscripts i can indicate the indices of both the time series for a single point and the spatial locations within the same wave field; thus, these parameters can be exhibited as climatological distributions for long-term statistics obtained from all regional points in the former situation or expressed as a series of values for a set of SWH fields in the latter.

2.4. Experimental design

The matrix of input feature elements was selected from the wind fields in the training dataset mentioned above, and each slice of the matrix comprised wind components in the u- and v-directions. In this study, 12 wind slices were employed for the 12 STE structures, covering the period from 72 h (T - 72 h) to 6 h (T - 6 h) with 6 h intervals, as mentioned in Section 2.2. Additionally, one more slice at T-0 h in the matrix was prepared for the IE. Therefore, the each simulation step in GWSM4C contains 26 wind components as inputs. Notably, the input u- and v-wind values of the land points were set to zero because land-based wind fields have no influence on wave.

The GWSM4C model was trained by using the MASNUM-WAM-simulated SWH and the corresponding ERA5 wind forcing from 2017 to 2020, with samples selected at 00:00 (UTC) of each day. Thus, the total training sample size is (3x365 + 366) = 1461. Each sample contains the gridded SWHs with the resolution of 291x720 covering global sea areas from 72.5°S to 72.5°N. The training input matrices comprised 1461 samples, 26 channels, 291 rows, and 720 columns. As an independent test, the SWH in 2021 output by GWSM4C was compared with that generated from the same wave modeling environment described above. The test interval was set to 3 h with the same resolution and coverage as the training grid. Consequently, the test sample size is (8x365) = 2920. The testing input matrices comprise the same number of channels, rows, and columns as the training matrices.

The influence of nearshore water depth on wave simulation is ignored in GWSM4C, i.e., only land and water points are identified, and all the relevant values of land points are set to zero. However, as the number of convolutional iterations increases, the zeros on land that are near water can be changed to nonzero values, thereby becoming noise in the convolutions of adjacent points. To resolve this problem, a mask algorithm is introduced, as specified in Section 4.1.

Notably, the latitude-longitude training matrix might introduce discrepancies in distance between low and high latitudes. The deviation might become more pronounced as wave approach the poles, and the variation in propagation distances in near-polar areas can lead to unavoidable bias in the distance between meridians. Furthermore, the inherent discontinuity of the matrix can enhance the magnitude of the error at the edges of the matrix. To alleviate this problem, an edge-filling approach is implemented during the convolution process. Using the "circular" padding method within PyTorch (Paszke et al., 2019), the data on the left and right and at the upper and lower borders are seamlessly connected, thereby efficiently alleviating boundary-related errors.

The Adam (Kingma and Ba, 2014) optimizer with $\beta_1 = 0.9$, $\beta_2 = 0.999$, and $\in = 10^{-8}$ was adopted in this study. The learning rate over the training process changes according to the following equations:

$$lf = \left(1 + \frac{\cos\left(\frac{\pi \cdot step}{step\_num}\right)}{2}\right)(1 - lrf) + lrf. \tag{12}$$

$$lr_{new} = lf \times lr \tag{13}$$

with $step\_num = 200$, $lrf = 0.1$, and $lr = 0.001$. Additionally, for network training, the mean squared error and He initialization (He et al., 2015) scheme were selected as the loss function and weight initialization, respectively.

GWSM4C was trained on a machine with four NVIDIA V100 GPUs (32 GB). The base models using the hyperparameters described above were trained for 200 epochs, the batch size during training was set to 1 and each training epoch required approximately 480 s.

3. Results

3.1. Validation and analysis of simulation results from GWSM4C

Fig. 3 shows the seasonally averaged SWH simulated by GWSM4C in comparison with that generated by MASNUM-WAM for 2021. It is evident that the RMSEs and CORs in most oceanic regions, extracted from the SWH time series at each computational grid, are <0.3 m and >0.9, respectively, and that the BIAS is within the range of ±0.2 m, reflecting a remarkable resemblance to the numerical model result. However, the similarity is less strong in both the Antarctic and Arctic Oceans. This poorer performance could be attributable to the much shorter distance between meridians (zonal lengths) at high latitudes compared with the preassigned $L_{dis} = 111$ km, as explained in Section 2.2.

Notably, less agreement is also evident between the GWSM4C and MASNUM-WAM results in equatorial regions, especially near the west coasts of the continents. The RMSE and bias in these areas reach 0.4 and 0.3 m, respectively, and the COR is as low as 0.6. Such discrepancies might be associated with the complexity of the wave systems that propagate northward and southward in those areas. Additionally, the equatorial region has relatively weak winds, hindering the formation of dominant wave systems; thus, understanding of wave behavior in such regions is more difficult for GWSM4C. Nevertheless, such a situation might be alleviated if winds from a much longer historical period are used as inputs (see Section 3.2 for further discussion).

To demonstrate the ability of GWSM4C to simulate different sea areas, the global ocean between 70°S and 70°N was divided into seven reference regions. As shown in Fig. 4, the regions were specified as the Northern Indian Ocean (NIO), Northern Pacific Ocean (NPO), and Northern Atlantic Ocean (NAO) on the northern side of the equator and as the Southern Indian Ocean (SIO), Tropical Pacific Ocean (TPO), and Tropical Atlantic Ocean (TAO) in the region 0°–35°S and as the Southern Ocean (SOO) from 35° to 70°S. The boundaries between the NIO and NPO and between the TPO and SIO were set at 100°E and 140°E, respectively.

Fig. 5 shows the SWH BIASs between GWSM4C and MASNUM-WAM, which are the averages for the months of March–May (Fig. 5a), June–August (Fig. 5b), September–November (Fig. 5c), December–February (Fig. 5d), and for the entire year (Fig. 5e) of 2021. In each panel, the BIASs derived from different reference regions are identified by lines in different colors and are presented corresponding to SWH values of 0–10 m. The vertical dashed lines in each panel indicate the percentiles of the SWH values. As shown in Figure, most of the regions present negative BIAS in a low sea state (SWH percentile <50%) but positive BIAS in a higher sea state (SWH percentile within 50%–90%). Moreover, positive BIAS values in extreme sea states (SWH percentile >99%) can be found in the SOO, NPO, and NAO regions. Generally, the prediction deviations under extreme sea conditions are more stable than those under moderate

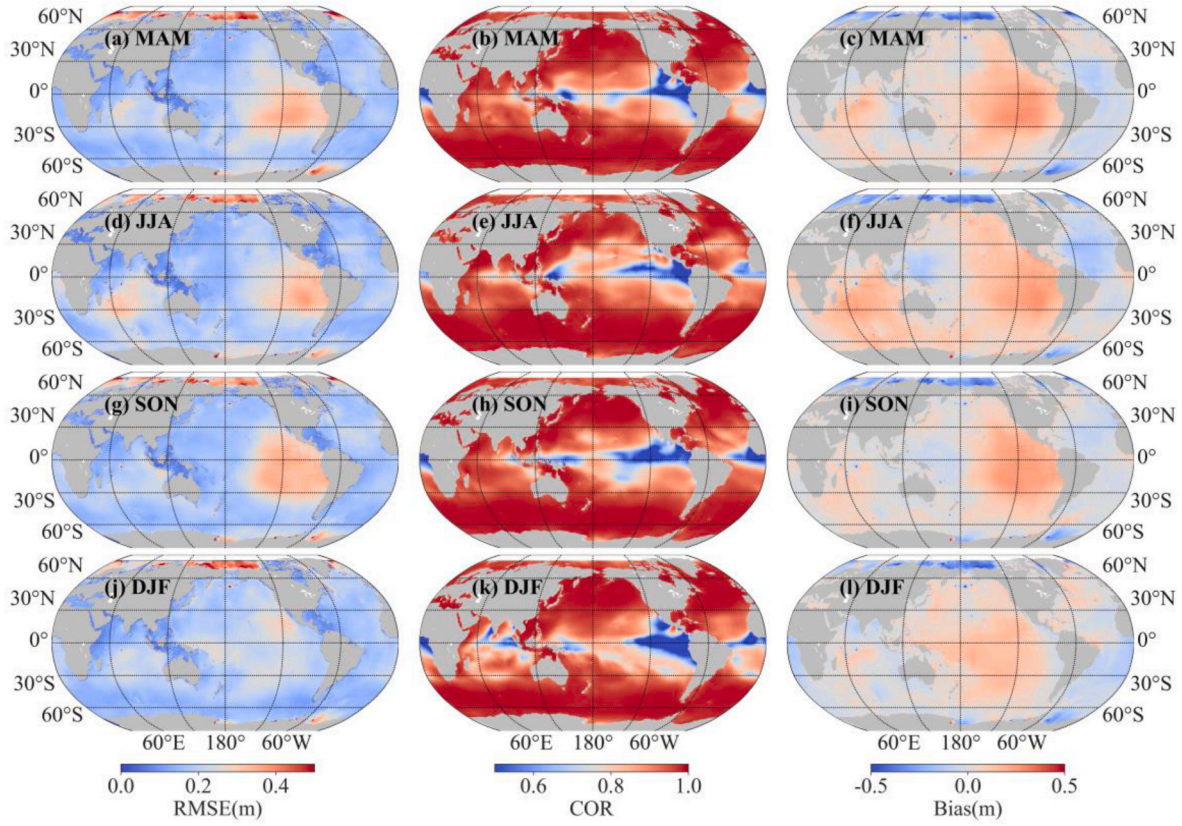

Fig. 3. Global climatological distribution of seasonally averaged (left) RMSE, (center) COR, and (right) BIAS in SWH in (a–c) March–May (MAM) 2021, (d–f) June–August (JJA) 2021, (g–i) September–November (SON) 2021, and (j–l) January, February, and December 2021 (DJF).

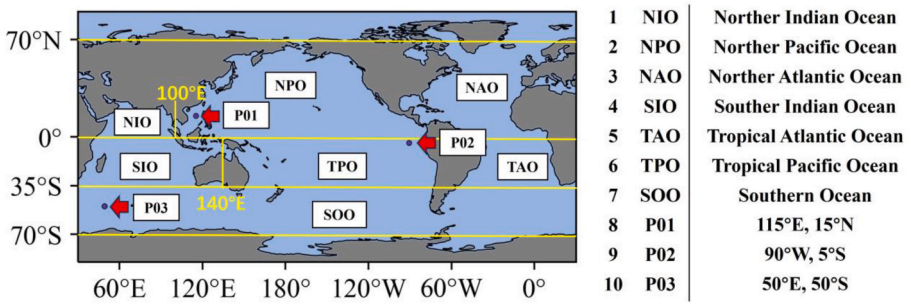

Fig. 4. Locations of the reference sea regions and points.

and low sea conditions. Overall, the results depicted in Fig. 5 show markedly higher BIAS values in the TPO area.

In addition, the one-year SWH time series derived for reference points P01, P02, and P03 (as shown in Fig. 4) are exhibited as single-point long-term series of GWSM4C performance in Fig. 6. The reference points were selected to represent waves with distinctly different characteristics. As shown in Fig. 6a, the scatter distribution between the GWSM4C-simulated SWH and MASNUM-WAM-simulated SWH reveals notable stability within the semienclosed marine region of the South China Sea (i.e., RMSE = 0.12, BIAS = −0.0058, and COR = 0.985). However, in the eastern equatorial Pacific Ocean dominated by multiple swells, there are obvious biases with underestimations compared with the criteria of the numerical model product, indicating the inability to capture the features of long-period waves in such sea areas (Fig. 6b). Nevertheless, the GWSM4C shows great learning capability in high sea states, as depicted in Fig. 6c. Notably, even for an SWH >6 m, the newly established model outputs accurate predictions. The model can maintain consistently good performance in the South China Sea and Southern Ocean regions over the whole year for testing, implying that GWSM4C is better at learning the characteristics of wind waves.

3.2. *Learning capability for complex sea states with multiple wave systems*

The poor performance at reference point P02, with lower accuracy and correlation (Fig. 6b), might be highly related to the complexity of the coexisting wave systems, whose behaviors are not well understood by GWSM4C. Furthermore, it was found from additional experiments that the learning ability in such sea states could be improved by extending the temporal span of the historical wind fields used as inputs.

Therefore, we conducted additional experiments concerning the temporal spans of the input winds (specifically, T - 60, T - 48, T - 36, T - 24, and T - 12 h), and each test corresponded to a specific number of STE structures (e.g., 10, 8, 6, 4, and 2), which decreased as the first historical wind field input became closer to the simulation moment (T - 0 h). The

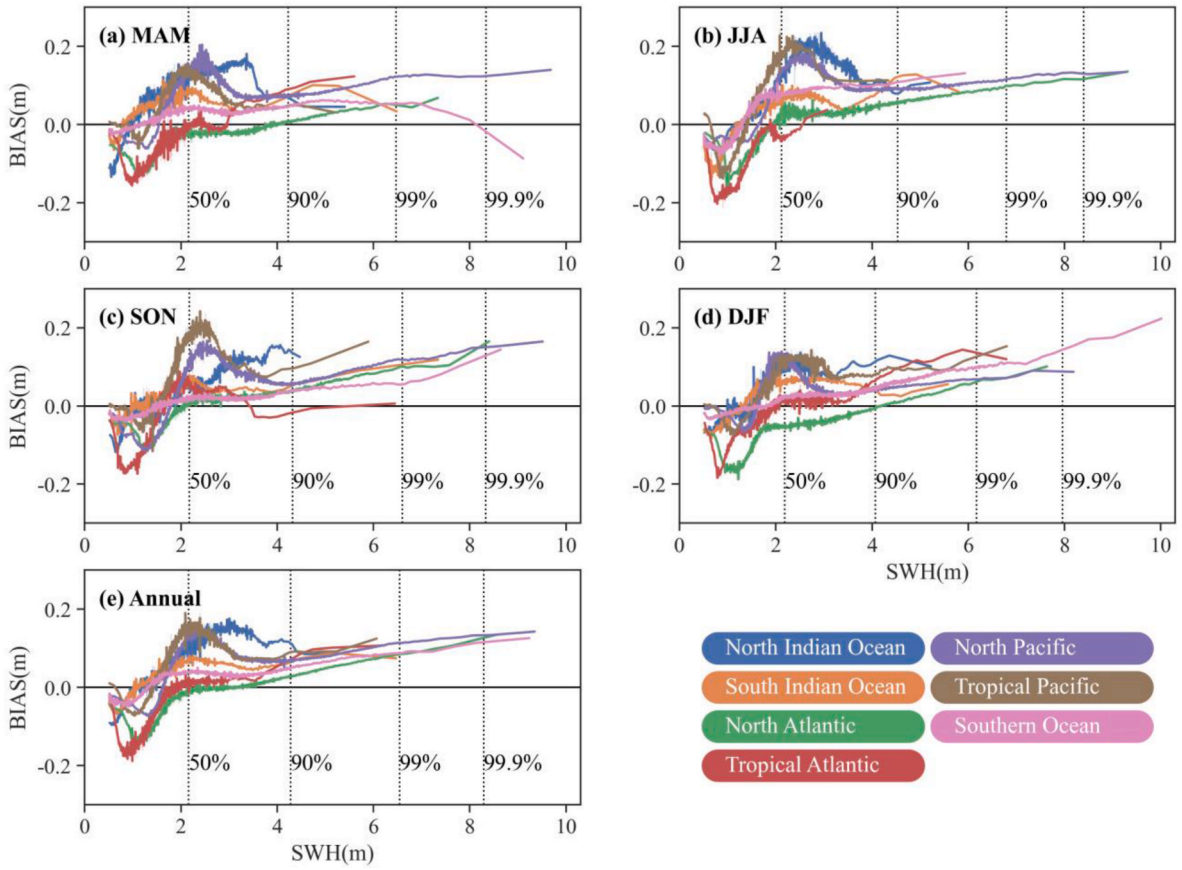

Fig. 5. Averaged SWH BIAS in (a) March–May (MAM), (b) June–August (JJA), (c) September–November (SON), (d) December–February (DJF), and (d) 2021. In each panel, the BIAS corresponding to the SWH values are presented, and the dashed vertical lines indicate the SWH percentiles.

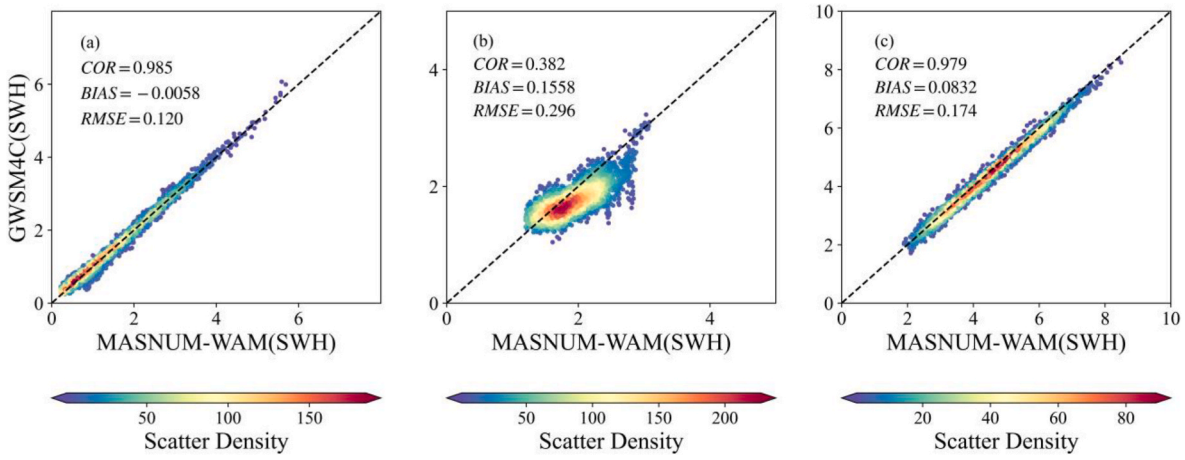

Fig. 6. Scatter plots of SWH at reference points (a) P01, (b) P02, and (c) P03, which are in the South China Sea, eastern equatorial Pacific Ocean, and region of the westerlies in the Southern Ocean, respectively. The color bar in each panel depicts the density of the scatter points, with redder (bluer) colors indicating richer (poorer) density.

other training/testing data and methods adopted in these experiments were the same as those described in Section 2.4. As shown in Fig. 7, which shows the RMSE, COR, and RE derived from the existing (T - 72 h) and additional tests, the RMSE and RE (COR) values increase (decrease) as the first historical wind input becomes closer, suggesting that the consideration of further wind slices and the adoption of more STE structures leads to better learning ability in deciphering complex wave systems. The same conclusion can be drawn following the analysis of Fig. 8, which presents the climatological distributions of the COR values derived from the T - 72 h experiment (Fig. 8a) and the additional tests (Fig. 8b–f). It is evident from Fig. 8 that the red shading covers a greater area of the global oceans, while the area of blue shading shrinks as the first historical wind input moves further away, indicating that the GWSM4C simulations can achieve higher levels of learning ability in more ocean regions. Moreover, the improvements are more notable at high and medium latitudes than at low latitudes, confirming that the greater complexity of multiple wave systems presents wave state features that are more difficult to learn. On the other hand, the results also

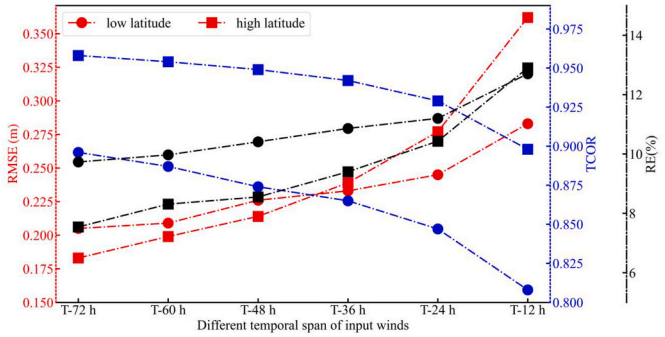

Fig. 7. Global annual averaged error parameters for different input-wind temporal spans. The red, blue, and black lines represent the RMSE, COR, and RE, respectively. Circular markers represent low latitudes, square markers represent high latitudes, and the x-axis represents the temporal span of the input winds.

suggest that GWSM4C can extract and learn the features of complex wave states by considering more historical wind inputs. However, the use of more historical wind input data can result in extremely high computational costs in the current version of GWSM4C; therefore, optimizing the efficiency of GWSM4C and improving the biases in equatorial regions will be the primary targets of our future studies.

4. Discussion

4.1. Strategy for values on land in the convolution operation

As mentioned in Section 2.4, all the relevant values at the land points were set to zero. However, because convolution operations inherently lack the capability to distinguish sea and land, the values on land regions adjacent to water could change to nonzero values during convolution operations, resulting in water variables traveling across narrow areas of land, such as peninsulas and capes.

A sea–land separation module was therefore developed to retard such a situation. By introducing a 2D mask ($M(i,j), i \in [1,w], j \in [1,h]$), the locations of land points can be marked, e.g., $M(i,j) = 0$ indicates that location (i,j) is on land. w and h in the introduced matrix denote the width and height of the input, respectively. After each convolution operation, the 3D output $O(k,i,j)$ might retain the same w and h as the input, but the number of components in the first dimension is equal to the number of kernels nk used in the previous convolution, i.e., $k \in [1, nk]$. In the retarding module, the output is checked with the mask immediately following each convolution operation, i.e., letting $O(k, i, j) = 0$, whereas $M(i,j) = 0$ for each k within $[1,nk]$. It is noteworthy that this module should be utilized in both the convolutional and BatchNorm layers.

The spatial distributions of the SWH propagation characteristics in the Central American region generated by MASNUM-WAM, GWSM4C with the retarding module, and GWSM4C without the retarding module are shown in Fig. 9a–c, respectively. It is evident that for wave energy propagating from the upper-right corner of the panel, the retarding procedure can prevent waves from propagating across the land, as shown by the similar shading and small wave heights in Fig. 9a and b, which contrast with the situation shown in Fig. 9c.

4.2. Cumulative error analysis

Cumulative error is one of most critical factors that limits current neural network models from performing long-term predictions because the cumulative errors increase rapidly during the forecast period (Fan et al., 2020; Zhou et al., 2021a). In our work, the initial wave states of GWSM4C for the prediction time are generated simultaneously with the wind fields at previous moments. Therefore, the errors due to the wave states will not increase as the simulation continues. To demonstrate this, a simulation experiment during two typhoon events was conducted.

A swath map of the maximum SWH in September 2021 simulated by MASNUM-WAM during the passages of the super typhoons CHANTHU and MINDULLE is presented in Fig. 10a. The regional mean SWH of the observations (black line), RMSE (red line) and COR (blue line) between

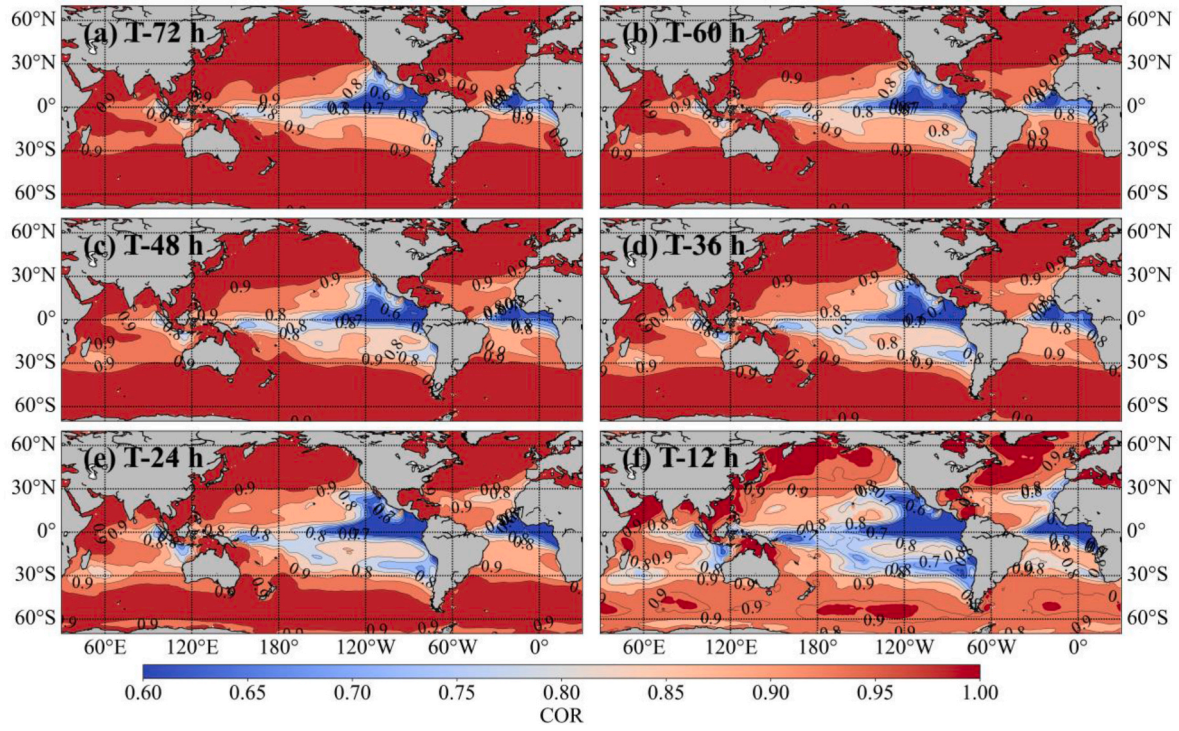

Fig. 8. Climatological distributions of the annual average COR derived from the existing and additional tests. The temporal span of the input winds is shown in the upper-left corner of each panel.

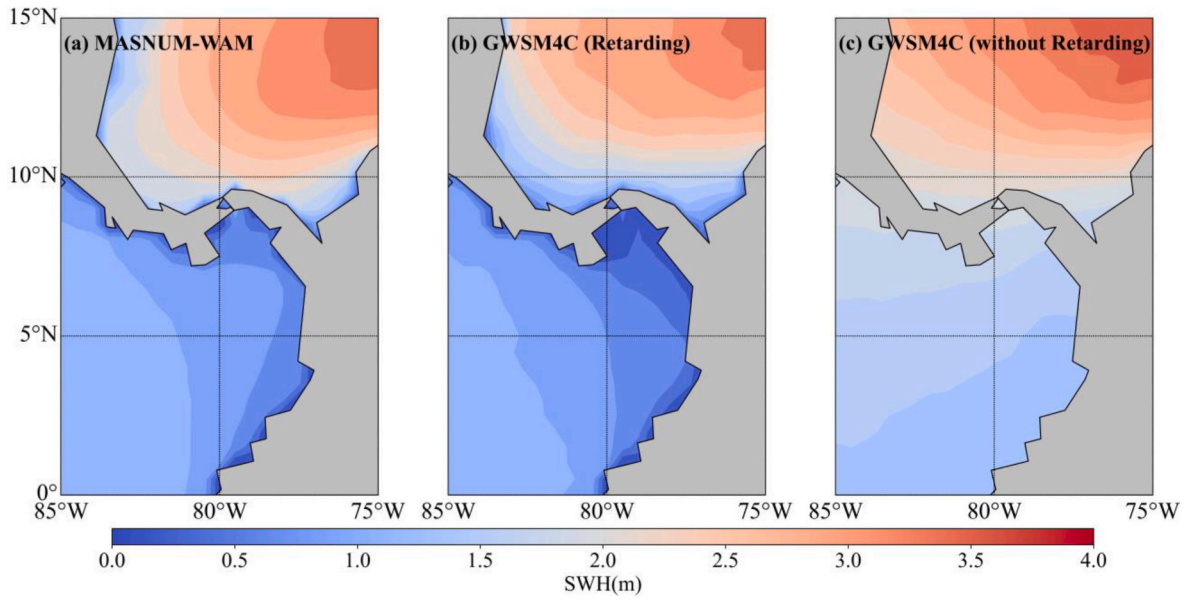

Fig. 9. Spatial distribution of SWH in the nearshore region of Central America: (a) MASNUM-WAM, (b) GWSM4C with the Retarding module, and (c) GWSM4C without the Retarding module. The color bar represents the SWH.

the observations and simulations from GWSM4C during typhoons CHANTHU and MINDULLE are presented in Fig. 10b. The RMSE and COR reached average values of 0.17 m (range: 0.09–0.35 m) and 0.997 (range: 0.994–0.999), respectively. The values of both do not present any trend of sustained increase, even during the periods of the super typhoons (as indicated by the yellow and green boxes in Fig. 10b). This special characteristic implies that GWSM4C can perform long-term simulations with acceptable and stable prediction errors and that such a deep-learning model could be adopted as a surrogate for the numerical wave models currently adopted in climatology-related research but with greatly reduced computational costs.

4.3. Applicability of other resolutions

GWSM4C can also conduct high-resolution simulations, i.e., produce SWHs with higher resolutions than those adopted in the training but without retraining. Such a simulation can be achieved using the dilated convolution approach with an appropriate dilation rate. As illustrated in Fig. 11a and b, by setting the dilation rate to a value of 2, the blue grids, which should be influenced by the central red grid over a single convolution, remain within the same scope but with the resolution changing from 0.5° × 0.5°–0.25° × 0.25°. However, such a convolution might cause the results of the current layer to constitute individual ensembles from the preceding layer, making them independent of each other and resulting in a loss of local information (Wang et al., 2018), as shown in Fig. 11d.

To resolve the gridding problem, a new optimization algorithm was developed. As illustrated in Fig. 11c, the signals of the red, yellow, blue, and green grids are first extracted individually and then interpolated to finer resolution, i.e., 0.25° × 0.25°, in this example. Then, the mean values of their overlapping regions are accepted as the final convolution results. Such an approach can rebuild the relationship between each dilated convolution, thereby retrieving the complete local information, as depicted in Fig. 11e.

The effectiveness of the newly developed algorithm was compared with the outputs of MASNUM-WAM and the original GWSM4C with a 0.25° resolution. In comparison with the original version, as shown in Fig. 12b, the optimized results (Fig. 12c) exhibit notable improvements in eliminating gridding problems and producing much smoother contour lines, which are comparable with those of the numerical model product (Fig. 12a).

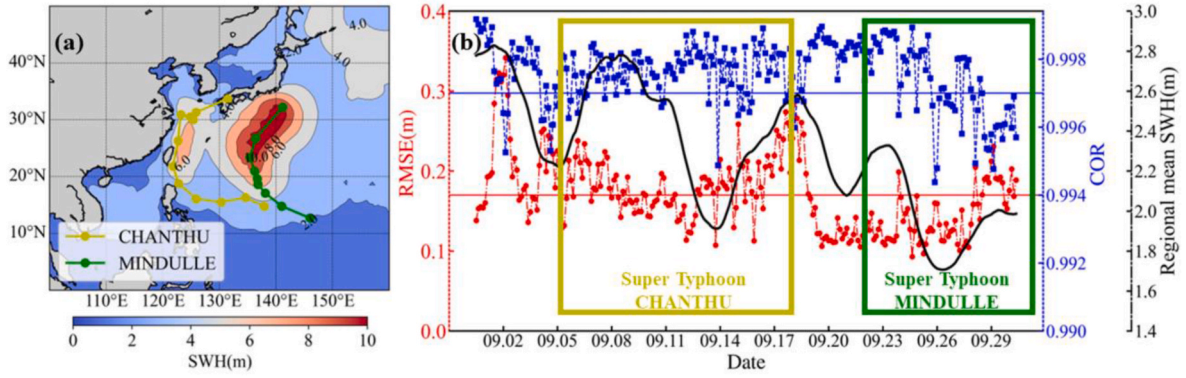

Fig. 10. Demonstration of the simulation results under two typhoon conditions: (a) swath map of the maximum MASNUM-WAM-simulated SWH during super typhoons CHANTHU and MINDULLE (whose paths are indicated by yellow and green lines, respectively) in September 2021, and (b) regional SWH (simulated by MASNUM-WAM, black line), regional RMSE (red line), and regional COR (blue line) in the region of 0°–50°N, 100°–160°E during September 2021. The periods of the super typhoons CHANTHU and MINDULLE are marked by yellow and green boxes, respectively.

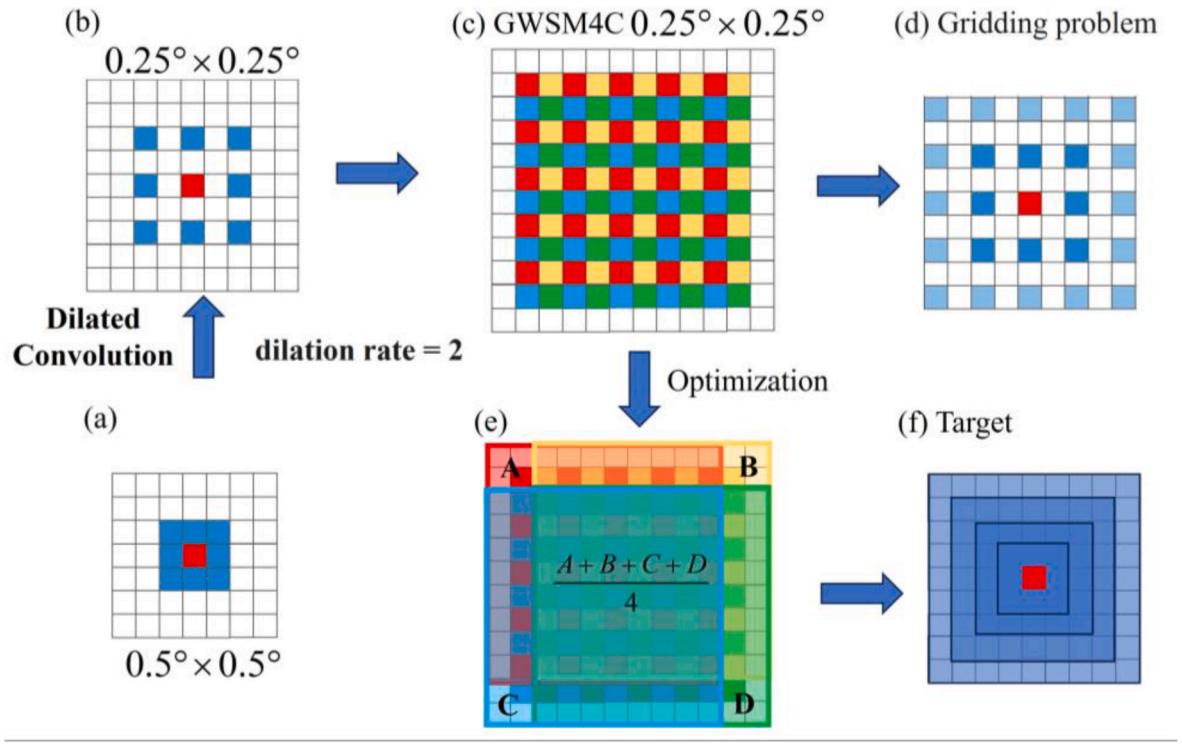

Fig. 11. GWSM4C application procedure at different resolutions.

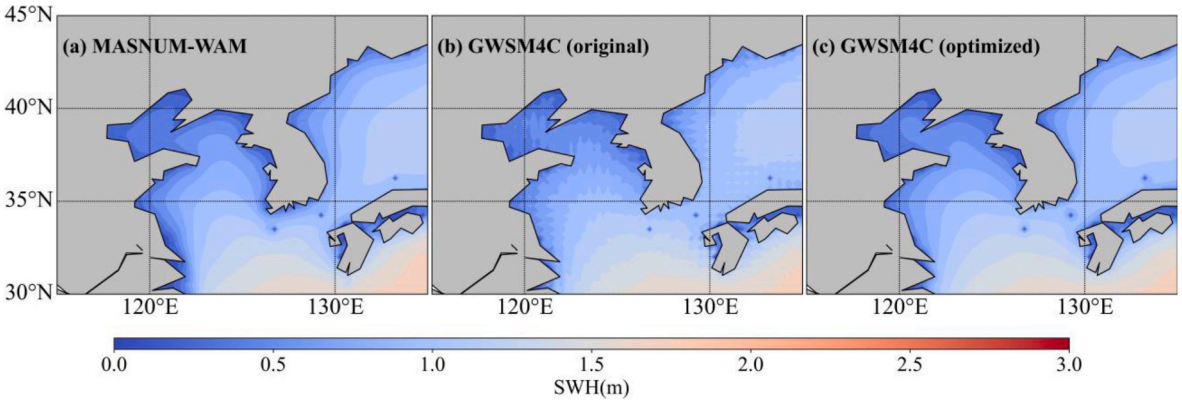

Fig. 12. Spatial distribution of SWH with 0.25° resolution: (a) MASNUM-WAM, (b) GWSM4C (original), and (c) GWSM4C (optimized). The color bar represents the SWH.

4.4. Application of GWSM4C

The purpose of this study is to develop an economical and feasible surrogate model to replace third-generation numerical wave models in climate models. Learning the forecast behaviors of a given third-generation wave model is the core of the newly established model, so the performance of the new model is strongly influenced by the property from which it learns from. Consequently, the training outcomes in this work are constrained by the performances of both the MASNUM-WAM and ERA5 winds, and the surrogate model requires a re-adaptation before its new application.

The GWSM4C model can forecast or hindcast significant wave heights similarly to third-generation wave models with corresponding forecast or hindcast winds as inputs. However, the accuracy of its product has only been validated for long-term climatological statistics. Therefore, the newly proposed model is presently considered for climate simulations.

5. Conclusions

This paper presents an economical and feasible surrogate model named GWSM4C, which can be applied to replace the current third-generation numerical wave models in various domains, e.g., climate modeling and wave climate analysis. The proposed model overcomes the most crucial limitation of existing deep learning wave prediction models, i.e., the limitation of long-term predictions. In addition, the newly proposed model can predict SWH prediction in large water areas, even in the global ocean.

We refined the original design principles of CNNs and aligned the traveling distances of waves with the size of the RF in each CNN layer, thereby creating a physically constrained CNN.

Following the three defining properties of CNNs proposed by LeCun et al. (1998), such as local RFs, shared weights (or weight replication), and spatial or temporal subsampling, the principles of the design of GWSM4C are as follows.

- First, the RF range in the CNN gradually expands outward during the convolution process, which is akin to the principle of ripple diffusion caused by a disturbance. This principle is adopted to describe wave propagation in the establishment of the new model.
- Second, weight sharing reduces the number of parameters, although it has additional importance in the proposed model. For example, for any given area and time in the global ocean, the results computed through a convolution share the same set of weights, conforming with the inherent principles of wave propagation.
- Finally, the proposed model does not employ temporal or spatial subsampling. Every convolution process in the model refrains from the subsampling step because this a step tends to discard valuable oceanographic information.

The initial conditions in GWSM4C simulations can be updated simultaneously, avoiding the accumulation of errors from a previous simulation wave state and making long-term simulation based on deep-learning algorithms possible. Furthermore, GWSM4C can easily port different resolutions and is free of truncation errors caused by model parallelism. Therefore, the integration of such a model as a surrogate wave model in a climate model is feasible in the future.

Although a GWSM4C simulation can capture the basic characteristics of the benchmark data mentioned above, biases can still be found in several ocean regions. For example, the seasonally averaged RMSE and COR values are slightly greater and lower, respectively, in equatorial regions, especially near the west coasts of continents, than in other parts of the ocean. These regions are renowned for their intricate coexisting wave systems, which are much more difficult for STEs to learn and emulate. However, the results of additional training tests suggested that the use of longer historical wind data could alleviate such discrepancies, although the associated computational costs might also increase. Therefore, optimization of GWSM4C with respect to computational efficiency will be a primary target in our future studies.

The current version of GWSM4C focuses on the global ocean. However, only land and sea points can be identified, and the refraction effects of water depth on wave propagation in nearshore areas are ignored. In future work, water depth elements could also be incorporated into model training, allowing GWSM4C to emulate the refraction of wave propagation in nearshore regions.

Data availability

The hourly ECMWF-ERA5 reanalysis data (https://doi.org/10.24381/cds.adbb2d47) can be downloaded from https://cds.climate.copernicus.eu/. Global significant wave height data for GWSM4C training and testing can be accessed through a private link https://www.scidb.cn/en/s/b67bYj or through the anonymous private link https://www.scidb.cn/en/anonymous/YjY3Yllq.

Code availability.

The GWSM4C source code will be provided upon request to replicate the results described in this paper. The code may be requested from the corresponding author via email.

CRediT authorship contribution statement

Quan Jin: Writing – original draft, Visualization, Validation, Software, Methodology, Investigation, Formal analysis. **Xingjie Jiang:** Writing – review & editing, Validation, Software, Formal analysis, Data curation. **Feng Hua:** Writing – review & editing, Validation, Methodology, Investigation. **Yongzeng Yang:** Writing – review & editing, Validation. **Shumin Jiang:** Writing – review & editing, Investigation. **Chen Yu:** Writing – review & editing, Resources, Methodology. **Zhenya Song:** Writing – review & editing, Writing – original draft, Supervision, Resources, Methodology, Funding acquisition, Formal analysis, Conceptualization.

Declaration of competing interest

The authors declare that they have no known competing financial interests or personal relationships that could have appeared to influence the work reported in this paper.

Acknowledgments

This research was funded by the National Natural Science Foundation of China (No. 41821004), the Basic Scientific Fund for National Public Research Institute of China (Shu-Xingbei Young Talent Program 2023S01), the National Key Research Program of China (No. 2021YFC3101600), the Open Research Fund of Guangdong Provincial Key Laboratory of Marine Disaster Prediction and Prevention (GPKLMD2023005), the Shantou University Scientific Research Funded Project (NTF21036), and the China–Korea Cooperation Project on Northwest Pacific Marine Ecosystem Simulation under Climate Change.

References

Alizadeh, M.J., Nourani, V., 2024. Multivariate GRU and LSTM models for wave forecasting and hindcasting in the southern Caspian Sea. Ocean Eng. 298, 117193.

Amante, C., Eakins, B.W., 2009. ETOPO1 1 Arc-Minute Global Relief Model: Procedures, Data Sources and Analysis. NOAA Technical Memorandum NESDIS NGDC-24. National Geophysical Data Center, NOAA. https://doi.org/10.7289/V5C8276M.

Bao, Y., Song, Z.Y., Qiao, F.L., 2020. FIO-ESM version 2.0: model description and evaluation. J. Geophys. Res. Oceans 125 (6), e2019JC016036. https://doi.org/10.1029/2019JC016036.

Bell, B., Hersbach, H., Simmons, A., Berrisford, P., Dahlgren, P., Horányi, A., Muñoz-Sabater, J., Nicolas, J., Radu, R., Schepers, D., Soci, C., Villaume, S., Bidlot, J., Haimberger, L., Woollen, J., Buontempo, C., Thépautet, J., 2021. The ERA5 global reanalysis: preliminary extension to 1950. Q.J.R. Meteorol. 147 (741), 4186–4227. https://doi.org/10.1002/qj.4174.

Booij, N., Ris, R.C., Holthuijsen, L.H., 1999. A third-generation wave model for coastal regions: 1. Model description and validation. J. Geophys. Res. Oceans 104 (C4), 7649–7666. https://doi.org/10.1029/98JC02622.

Cavaleri, L., Barbariol, F., Benetazzo, A., Bertotti, L., Bidlot, J.R., Janssen, P., Wedi, N., 2016. The Draupner wave: a fresh look and the emerging view. J. Geophys. Res. Oceans 121 (8), 6061–6075. https://doi.org/10.1002/2016JC011649.

Dong, G.H., Zheng, Z.J., Ma, X.Z., Huang, X.Z., 2020. Characteristics of low-frequency oscillations in the Hambantota Port during the southwest monsoon. Ocean Eng. 208, 107408 https://doi.org/10.1016/j.oceaneng.2020.107408.

Fan, S., Xiao, N., Dong, S., 2020. A novel model to predict significant wave height based on long short-term memory network. Ocean Eng. 205, 107298 https://doi.org/10.1016/j.oceaneng.2020.107298.

Feng, Z.J., Hu, P., Li, S.Q., Mo, D.X., 2022. Prediction of significant wave height in offshore China based on the machine learning method. J. Mar. Sci. Eng. 10 (6), 836. https://doi.org/10.3390/jmse10060836.

Hasselmann, S., Hasselmann, K., 1985. Computations and parameterizations of the nonlinear energy transfer in a gravity-wave spectrum. Part I: a new method for efficient computations of the exact nonlinear transfer integral. J. Phys. Oceanogr. 15 (11), 1369–1377. https://doi.org/10.1175/1520-0485(1985)015<1369:CAPOTN>2.0.CO;2.

Hasselmann, S., Hasselmann, K., Allender, J.H., Barnett, T.P., 1985a. Computations and parameterizations of the nonlinear energy transfer in a gravity-wave spectrum. Part II: parameterizations of the nonlinear energy transfer for application in wave models. J. Phys. Oceanogr. 15 (11), 1378–1391. https://doi.org/10.1175/1520-0485(1985)015<1378:CAPOTN>2.0.CO;2.

He, K.M., Zhang, X.Y., Ren, S.Q., Sun, J., 2015. Delving deep into rectifiers: surpassing human-level performance on imagenet classification. IEEE Int. Conf. Comput. Vis. 1026–1034. https://doi.org/10.1109/ICCV.2015.123.

Hemer, M.A., Wang, X.L., Weisse, R., Swail, V.R., 2012. Advancing wind-waves climate science: the COWCLIP project. Bull. Am. Meteorol. Soc. 93 (6), 791–796. https://doi.org/10.1175/BAMS-D-11-00184.1.

Hersbach, H., Bell, B., Berrisford, P., Hirahara, S., Horányi, A., Muñoz-Sabater, J., Nicolas, J., Peubey, C., Radu, R., Schepers, D., Simmons, A., Soci, C., Abdalla, S., Abellan, X., Balsamo, G., Bechtold, P., Biavati, G., Bidlot, J., Bonavita, M., Chiara, G. D., Dahlgren, P., Dee, D., Diamantakis, M., Dragani, R., Flemming, J., Forbes, R., Fuentes, M., Geer, A., Haimberger, L., Healy, S., Hogan, R.J., Hólm, E., Janisková, M., Keeley, S., Laloyaux, P., Lopez, P., Lupu, C., Radnoti, G., Rosnay, P., Rozum, I., Vamborg, F., Villaume, S., Thépaut, J., 2020. The ERA5 global reanalysis. Q.J.R. Meteorol. 146 (730), 1999–2049. https://doi.org/10.1002/qj.3803.

James, S.C., Zhang, Y., O'Donncha, F., 2018. A machine learning framework to forecast wave conditions. Coast Eng. 137, 1–10. https://doi.org/10.1016/j.coastaleng.2018.03.004.

Jiang, B., Wei, Y.L., Jiang, X.J., Wang, H.F., Wang, X.Y., Ding, J., Zhang, R., Shi, Y., Cai, X.Q., Wu, Y., 2016. Assessment of wave energy resource of the Bohai Sea, Yellow Sea and East China Sea based on 10-year numerical hindcast data[C]. In: Proceedings of the OCEANS 2016-Shanghai. IEEE, pp. 1–9. https://doi.org/10.1109/OCEANSAP.2016.7485434.

Jiang, X.J., Xie, B.T., Bao, Y., Song, Z.Y., 2023. Global 3-hourly wind-wave and swell data for wave climate and wave energy resource research from 1950 to 2100. Sci. Data 10 (1), 225. https://doi.org/10.1038/s41597-023-02151-w.

Kingma, D., Ba, J., 2014. Adam: a method for stochastic optimization. Comput. Sci. 30, 1272–1282. https://doi.org/10.48550/arXiv.1412.6980.

LeCun, Y., Bottou, L., Bengio, Y., Haffner, P., 1998. Gradient-based learning applied to document recognition[C]. Proc. IEEE 86 (11), 2278–2324. https://doi.org/10.1109/5.726791.

Liu, Q.X., Babanin, A., Fan, Y.L., Zieger, S., Guan, C.L., Moon, I.J., 2017. Numerical simulations of ocean surface waves under hurricane conditions: assessment of existing model performance. Ocean Model. 118, 73–93. https://doi.org/10.1016/j.ocemod.2017.08.005.

Luo, W., Li, Y., Urtasun, R., Zemel, R., 2016. Understanding the effective receptive field in deep convolutional neural networks. Adv. Neural Inf. Process. Syst. 29 https://doi.org/10.48550/arXiv.1701.04128.

Magnusson, K.A., Donelan, M.A., 2013. The Andrea wave characteristics of a measured North Sea rogue wave. J. Offshore Mech. Arct. 135 (3), 031108 https://doi.org/10.1115/1.4023800.

Paszke, A., Gross, S., Massa, F., Lerer, A., Bradbury, J., Chanan, G., Killeen, T., Lin, Z., Gimelshein, N., Antiga, L., Desmaison, A., Köpf, A., Yang, E., DeVito, Z., Raison, M., Tejani, A., Chilamkurthy, S., Steiner, B., Fang, L., Bai, J., Chintala, S., 2019. Pytorch: an imperative style, high-performance deep learning library. Adv. Neural Inf. Process. Syst. 32 https://doi.org/10.48550/arXiv.1912.01703.

Pierson Jr, W.J., Moskowitz, L., 1964. A proposed spectral form for fully developed wind seas based on the similarity theory of SA Kitaigorodskii. J. Geophys. Res. 69 (24), 5181–5190. https://doi.org/10.1029/JZ069i024p05181.

Qiao, F.L., Zhao, W., Yin, X.Q., Huang, X.M., Liu, X., Shu, Q., Wang, G.S., Song, Z.Y., Li, X.F., Liu, H.X., Yang, G.W., Yuan, Y.L., 2016. A highly effective global surface wave numerical simulation with ultra-high resolution[C]. In: Proceedings of the International Conference for High Performance Computing, Networking, Storage and Analysis (SC '16), 2016. IEEE Press, Piscataway, NJ, USA, p. 11. https://doi.org/10.1109/SC.2016.4. Article 5.

Qiao, F.L., Wang, G.S., Khokiattiwong, S., Akhir, M.F., Zhu, W.X., Xiao, B., 2019. China published ocean forecasting system for the 21st-Century Maritime Silk Road on December 10, 2018. Acta Oceanol. Sin. 38, 1–3. https://doi.org/10.1007/s13131-019-1365-y.

Ris, R.C., Holthuijsen, L.H., Booij, N., 1999. A third-generation wave model for coastal regions: 2. Verification. J. Geophys. Res. Oceans 104 (C4), 7667–7681. https://doi.org/10.1029/1998JC900123.

Rogers, W.E., Babanin, A.V., Wang, D.W., 2012. Observation-consistent input and whitecapping dissipation in a model for wind-generated surface waves: description and simple calculations. J. Atmos. Ocean. Technol. 29 (9), 1329–1346. https://doi.org/10.1175/JTECH-D-11-00092.1.

Soares, C.G., Cherneva, Z., Antão, E.M., 2003. Characteristics of abnormal waves in North Sea storm sea states. Appl. Ocean Res. 25 (6), 337–344. https://doi.org/10.1016/j.apor.2004.02.005.

Sun, M., Yin, X.Q., Yang, Y.Z., Wu, K.J., 2017. An effective method based on dynamic sampling for data assimilation in a global wave model. Ocean Dynam. 67, 433–449. https://doi.org/10.1007/s10236-017-1030-y.

Tamura, H., Waseda, T., Miyazawa, Y., 2009. Freakish sea state and swell-windsea coupling: numerical study of the Suwa-Maru incident. Geophys. Res. Lett. 36 (1) https://doi.org/10.1029/2008GL036280.

Tolman, H.L., 1991. A third-generation model for wind waves on slowly varying, unsteady, and inhomogeneous depths and currents. J. Phys. Oceanogr. 21 (6), 782–797. https://doi.org/10.1175/1520-0485(1991)021<0782:ATGMFW>2.0.CO;2.

Tolman, H.L., Chalikov, D., 1996. Source terms in a third-generation wind wave model. J. Phys. Oceanogr. 26 (11), 2497–2518. https://doi.org/10.1175/1520-0485(1996)026<2497:STIATG>2.0.CO;2.

Trulsen, K., Nieto Borge, J.C., Gramstad, O., Aouf, L., Lefèvre, J.M., 2015. Crossing sea state and rogue wave probability during the Prestige accident. J. Geophys. Res. Oceans 120 (10), 7113–7136. https://doi.org/10.1002/2015JC011161.

WAMDI Group, 1988. The WAM model-a third generation ocean wave prediction model. J. Phys. Oceanogr. 18, 1775–1810. https://doi.org/10.1175/1520-0485(1988)018<1775:TWMTGO>2.0.CO;2.

Wang, G.S., Zhao, C., Xu, J.L., Qiao, F.L., Xia, C.S., 2016. Verification of an operational ocean circulation-surface wave coupled forecasting system for the China's seas. Acta Oceanol. Sin. 35, 19–28. https://doi.org/10.1007/s13131-016-0810-4.

Wang, P.Q., Chen, P.F., Yuan, Y., Liu, D., Huang, Z.H., Hou, X.D., Cottrell, G., 2018. Understanding convolution for semantic segmentation[C]. 2018 IEEE Winter Conference on Applications of Computer Vision (WACV). IEEE. https://doi.org/10.48550/arXiv.1702.08502.

Wang, G., Stanis, Z.E.O.G., Fu, D.J., Zheng, J.H., Gao, J.L., 2020. An analytical investigation of oscillations within a circular harbor over a Conical Island. Ocean Eng. 195, 106711 https://doi.org/10.1016/j.oceaneng.2019.106711.

Wang, L.N., Deng, X.L., Ge, P., Dong, C.M., Bethel, B.J., Yang, L.Q., Xia, J.Y., 2022. CNN-BiLSTM-Attention model in forecasting wave height over south−east China seas. CMC-Comput. Mater. Con. 73 (1), 2151–2168. https://doi.org/10.32604/cmc.2022.027415.

Waseda, T., Tamura, H., Kinoshita, T., 2012. Freakish sea index and sea states during ship accidents. J. Mar. Sci. 17, 305–314. https://doi.org/10.1007/s00773-012-0171-4.

Waseda, T., In, K., Kiyomatsu, K., Tamura, H., Miyazawa, Y., Iyama, K., 2014. Predicting freakish sea state with an operational third-generation wave model. Nat. Hazards Earth Syst. Sci. 14 (4), 945–957. https://doi.org/10.5194/nhess-14-945-2014.

Wessel, P., Smith, W.H., 1996. A global, self-consistent, hierarchical, high-resolution shoreline database. J. Geophys. Res. 101 (B4), 8741–8743. https://doi.org/10.1029/96JB00104.

Young, I.R., Ribal, A., 2019. Multiplatform evaluation of global trends in wind speed and wave height. Science 364 (6440), 548–552. https://doi.org/10.1126/science.aav9527.

Yuan, Y.L., Hua, F., Pan, Z.D., Sun, L.T., 1991. LAGDF-WAM numerical wave model - I. basic physical model. Acta Oceanol. Sin. 10 (4), 483–488.

Yuan, Y.L., Hua, F., Pan, Z.D., Sun, L.T., 1992. LAGFD-WAM numerical wave model - II: characteristics inlaid scheme and its application. Acta Oceanol. Sin. 11 (1), 13–23.

Zhou, S.Y., Bethel, B.J., Sun, W.J., Zhao, Y., Xie, W.H., Dong, C.M., 2021a. Improving Significant Wave Height Forecasts Using a Joint Empirical Mode Decomposition-Long Short-Term Memory Network. J. Mar. Sci. Eng. 9, 744. https://doi.org/10.3390/jmse9070744.

Zhou, S.Y., Xie, W.H., Lu, Y.X., Wang, Y.L., Zhou, Y.L., Hui, N., Dong, C.M., 2021b. ConvLSTM-based wave forecasts in the South and East China seas. Front. Mar. Sci. 8, 680079 https://doi.org/10.3389/fmars.2021.680079.

Zieger, S., Babanin, A.V., Rogers, W.E., Young, I.R., 2015. Observation-based source terms in the third-generation wave model WAVEWATCH. Ocean Model. 96, 2–25. https://doi.org/10.1016/j.ocemod.2015.07.014.